INT. J. NUM. METH. HEAT FLUID FLOW, VOL. 6 NO. 2, 3–24 (1996)

COMPUTER SIMULATION OF LIQUID ENCAPSULATED VERTICAL BRIDGMAN CRYSTAL GROWTH: PSEUDO STEADY-STATE CALCULATIONS

C. W. LAN and C. C. TING

Chemical Engineering Department, National Central University, Chung-Li, Taiwan 32054, ROC

ABSTRACT

A pseudo steady-state model is developed to study heat transfer, fluid flow, and the interface shape in the liquid encapsulated vertical Bridgman crystal growth. The model, which is governed by momentum, heat, and overall mass balances in the system, is solved by a finite-volume/Newton method. Flow and temperature fields, as well as unknown melt/crystal and melt/encapsulant interfaces, are calculated simultaneously. Sample calculations are mainly conducted for the $GaAs/B_2O_3/PBN$ system. Calculated results for the Germanium/graphite system are compared with finite element calculations by Adornato and Brown, and they are in good agreement. The effects of some process parameters, including the growth speed, ambient temperature profile and heat transfer conditions, on flow patterns, temperature fields and the interface shape are illustrated through calculated results. Interface inversion from concave to convex, by modifying the ambient temperature profile, is also demonstrated through computer simulation. Particularly, through an inverse problem approach, a flat interface can be easily obtained for various operation conditions.

KEY WORDS Crystal growth Vertical Bridgman Heat transfer Finite volume Newton method

INTRODUCTION

The Vertical Bridgman (VB) process has been used widely for growing high quality III-V semiconductors such as *GaAs*, *InP*, and *GaP*, etc. For these materials, to maintain the stoichiometry of compounds, a liquid encapsulant, such as B_2O_3, is usually used to prevent volatilization of components. Recently, the liquid encapsulated vertical Bridgman (LEVB) grown *GaAs*, *InP*, and *GaP* crystals with large diameter and low dislocation density have been reported[1–6]. In fact, different furnace designs for the VB method have led to different names for the process, for example, the vertical dynamic gradient freeze (VDGF) technique for which an electrodynamic gradient multi-zone furnace is used to simulate the motion of ampoule or furnace[2–4]. However, they can all, conceptually, be grouped into the same category of the VB process. As compared with the Czochralski method (Cz), the LEVB technique may provide a more ecomomical way to produce high quality crystals, because of its lower capital investment and less clean-up effort after crystal growth. In fact, recent reports[2–4] have shown that VDGF grown *GaAs* and *InP* single crystals have a much lower dislocation density than those grown from the Cz process. Nevertheless, similar to other crystal growth processes, the control of the melt/crystal interface, which is governed by heat transfer and fluid flow during solidification, in the LEVB process is of prime importance. A flat or slightly convex interface shape toward the melt during crystal growth is most desirable for growing single crystals with low defects[7]. A concave interface usually induces the growth of polycrystalline and thus degrades crystal quality.

0961–5539/96/020003–22$2.00

Received July 1994
Revised October 1994

However, during crystal growth, it is difficult to monitor the interface morphology. Therefore, numerical simulation of heat flow during crystal growth is necessary for providing useful information for process design and operation. Consequently, numerous computational studies have been devoted to this area in the past decade [e.g., References 8–20].

In most of numerical studies for VB crystal growth[8–13], a pseudo steady-state was assumed, and the encapsulant was not considered. Recently, Kim and Brown[14–16] developed a transient model based on the finite element analysis to study detailed convection and solute segregation in an ideal VB growth of III-V and II-VI compound semiconductors. Hofmann *et al.*[17] also used an unsteady state finite element model to study global heat and mass transfer in the VDGF process for 2-inch Germanium crystals. Melt/crystal interface inversion, from concave to convex, was also illustrated. Again the encapsulant was not included in these studies as well. In a recent study by Suzuki *et al.*[18], a simplified conduction model was used to study heat transfer in LEVB *GaAs* crystal growth, in which the encapsulant and the anisotropic ampoule were included. However, no fluid fluid was considered. Among these studies, most of results show a concave melt/crystal interface, except those results by Crochet *et al.*[12] and Hofmann *et al.*[17], in which the temperature profiles generated by a multi-zone furnace were adopted. Apparently, the control of interface convexity by the temperature profile from a traditional two-zone furnace has not been discussed. Also, all of the numerical studies mentioned were all based on the finite element method (FEM). Other numerical approaches, such as finite difference and finite volume methods, etc., for this free or moving boundary problem have not been used. Again, physical boundaries for the melt and encapsulant levels were assumed fixed. However, before crystal growth only initial amount of charge (material to be grown and encapsulant) is known. Therefore, to model the system in a self-consistent manner, the melt and the encapsulant levels, which are coupled with the position and the shape of the melt/crystal interface, need to be calculated. Furthermore, some fundamental issues, such as the effects of process parameters on flow patterns and the interface shape, have not been thoroughly discussed. Although some inverse problem approaches[19–20] have been proposed for obtaining a flat interface, in these models, however, only simple conductive heat transfer is considered.

In this report, a pseudo steady-state model is proposed to study LEVB crystal growth. This model will be validated by comparing calculated results with those from previous literature. The effects of some system parameters, particularly, the growth rate and ambient temperature distribution will be illustrated by calculated results. Interface control by modifying the ambient temperature distribution for the traditional two-zone furnace will also be illustrated through the model. More importantly, an inverse problem approach is also used to obtain a flat interface under various operation conditions. It should be pointed out that although a fully transient model is capable of providing more information about the system, particularly, the transient behavior, it needs much more CPU time and memory than steady-state models. Therefore, for a model-based crystal growth system, the steady-state model is more suitable for real-time computing and control.

MODEL DESCRIPTION

The LEVB crystal growth is simulated using a pseudo steady-state model. The model mainly neglects the evolution of system caused by the displacement of the ampoule in the furance. This approximation is usually valid at the middle of growth, in which end effects may be neglected. When a pseudo steady-state is achieved, if the ampoule is pulled downward at a speed U_{amp}, the crystal growth rate can be set to be U_{amp}. If the heating is axisymmetric, the physical domain of the model, which consists of encapsulant, melt, crystal, and ampoule, can be taken as shown in *Figure 1*. Due to axisymmetry, it can be treated as a two-dimensional model. Also, the mass of encapsulant and material, m_e and m_o, is known before growth, whereas the height of the melt/encapsulant interface is unknown *a priori*, and depends on the relative amount of the melt and the crystal, as well as the melt/crystal interface shape during crystal growth. The

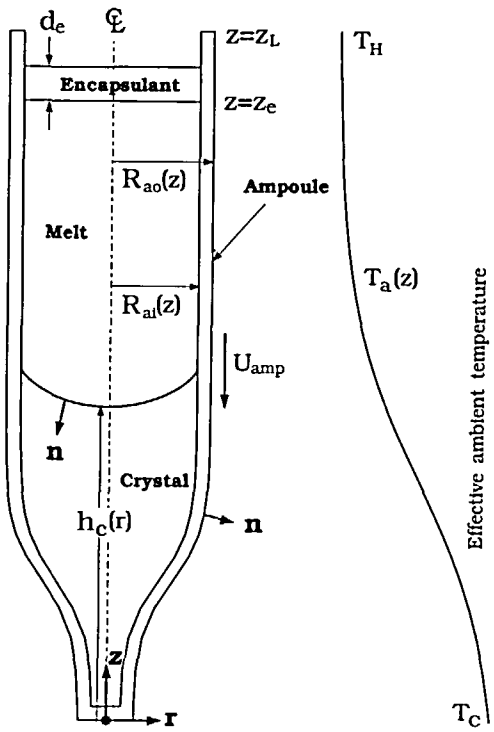

Figure 1 Schematic sketch for liquid encapsulated vertical Bridgman (LEVG) crystal growth system

melt/encapsulant interface and the top surface of the encapsulant are assumed flat for simplicity. Internal radiation inside the crystal and the radiation through the encapsulant, which is transparent, are not considered in the present study. The ampoule is also assumed isotropic. Again, due to the axisymmetry, the flow and temperature fields, as well as the heights of the encapsulant/melt (z_e) and melt/crystal ($h_c(r)$) interfaces, are represented in cylindrical coordinate system (r, z).

In this report, the melt is assumed incompressible and Newtonian, while the flow is laminar. Also, the Boussinesq approximation is adopted. As such, in the melt the governing equations in the conservative-law form (or the so-called divergence form) for fluid flow and heat transfer can be described in terms of stream function ψ, vorticity ω, and temperature T as follows:

Equation of motion

$$\frac{\partial}{\partial r}\left(\frac{\omega}{r}\frac{\partial \psi}{\partial z}\right)-\frac{\partial}{\partial z}\left(\frac{\omega}{r}\frac{\partial \psi}{\partial r}\right)+\frac{\partial}{\partial r}\left(\frac{1}{r}\frac{\partial}{\partial r}(\mu r\omega)\right)+\frac{\partial}{\partial z}\left(\frac{1}{r}\frac{\partial}{\partial z}(\mu r\omega)\right)-\rho_L\beta_T g\frac{\partial T}{\partial r}=0 \tag{1}$$

Stream equation

$$\frac{\partial}{\partial z}\left(\frac{1}{\rho_L r}\frac{\partial \psi}{\partial z}\right)+\frac{\partial}{\partial r}\left(\frac{1}{\rho_L r}\frac{\partial \psi}{\partial r}\right)+\omega=0 \tag{2}$$

Energy equation

$$-\frac{\partial}{\partial r}(\rho_i C_{pi} r u T)-\frac{\partial}{\partial z}(\rho_i C_{pi} r v T)+\frac{\partial}{\partial z}\left(rk_i\frac{\partial T}{\partial z}\right)+\frac{\partial}{\partial r}\left(rk_i\frac{\partial T}{\partial r}\right)=0, \qquad i=(e, L, s, a) \tag{3}$$

where μ is the viscosity of the melt, ρ_i the density, C_{pi} the specific heat, and k_i the thermal conductivity of phase i, where i represents for the encalpsulant (e), melt (L), crystal (s), and ampoule (a). Also, g is the gravity acceleration and β_T the thermal expansion coefficient of melt. The stream function ψ and vorticity ω in the above equations are defined in terms of the radial velocity u and axial velocity v as:

$$u=-\frac{1}{\rho_L r}\frac{\partial\psi}{\partial z}, \qquad v=\frac{1}{\rho_L r}\frac{\partial\psi}{\partial r}, \tag{4}$$

$$\omega=\frac{\partial u}{\partial z}-\frac{\partial v}{\partial r} \tag{5}$$

Again, since the ampoule is pulled downward at a speed U_{amp}, $v=U_{amp}$ and $u=0$ for the crystal, ampoule, and encapsulant.

The thermal boundary conditions are as follows:

1) Along the centerline,

$$\partial T/\partial r=0 \tag{6}$$

due to symmetry.

2) At the melt/encapsulant interface, the interfacial energy balance is,

$$k(\mathbf{n}\cdot\nabla T)|_L-k(\mathbf{n}\cdot\nabla T)|_e=0 \tag{7}$$

where $\mathbf{n}$ is the unit normal vector pointing into the encapsulant. It should be pointed out that in reality the radiation exchanges through the transparent encapsulant could be important. However, because the hot-zone temperature is usually uniform in the VB furnace, the radiation exchanges from the melt surface through the encapsulant to the furnace are small, and may be neglected.

3) At the melt/crystal interface, the interfacial energy balance is,

$$k(\mathbf{n}\cdot\nabla T)|_L-k(\mathbf{n}\cdot\nabla T)|_s+\rho_s\Delta H U_{amp}\mathbf{n}\cdot\mathbf{e}_z=0 \tag{8}$$

where $\mathbf{n}$ is the unit normal vector pointing into the crystal, $\mathbf{e}_z$ the unit vector in z-direction, and ΔH the heat of fusion. The temperature at the melt/crystal interface is set to the equilibrium melting point,

$$T=T_m \tag{9}$$

4) At the material/ampoule interface, the energy balance is,

$$k(\mathbf{n}\cdot\nabla T)|_i-k(\mathbf{n}\cdot\nabla T)|_a=0 \tag{10}$$

where $\mathbf{n}$ is the unit normal vector pointing into the ampoule and i the encapsulant (e), melt (L) and crystal (s).

5) Heat transfer from the system to the ambient is by both radiation and convection according to the energy balance along the ampoule surface:

$$-k(\mathbf{n}\cdot\nabla T)|_a=h(T-T_a)+\varepsilon_a\sigma(T^4-T_a^4) \tag{11}$$

where $\mathbf{n}$ is the normal vector on the ampoule pointing outwards, ε_a the emissivity of ampoule, σ the Stefan-Boltzmann constant, and T_a the effective ambient temperature.

6) At the top of the system, including the top surfaces of ampoule and encapsulant and the inner surface of the ampoule above the encapsulant surface, an adiabatic condition is used,

$$\mathbf{n}\cdot\nabla T=0 \tag{12}$$

Heat loss from the top surface can be added if necessary. However, in practice, a radiation shield is usually used, so that the heat loss from the top is small.

The heat exchanges between the surrounding (furnace) and the ampoule are dictated by an effective ambient temperature $T_a(z)$ specified along the ampoule surface. The effective ambient temperature distribution due to the two-zone VB furnace is assumed as follows:

$$T_a(z)=T_C+0.5(T_H-T_C)[1+\tanh[a(z-z_p)]/\tanh(0.5az_L)] \tag{13}$$

where T_H and T_C are approximately the hot- and cold-zone temperatures, respectively. z_p is the position of $0.5(T_H+T_C)$, a the parameter to adjust the gradient of distribution, and z_L the length of the ampoule. In practice, to obtain $T_a(z)$ it requires detailed modelling of the whole system, including the loaded materials and the furance. Indeed, the material used and the design of the furnace, as well as the presence of the ampoule, can affect the thermal environments significantly, which in turn affect the effective ambient temperature profile. However, in the present study for simplicity $T_a(z)$ is assumed to be a known independent variable.

The fluid-flow boundary conditions are as follows:

1) Along the centerline

$$\psi=0, \qquad \omega=0 \tag{14}$$

where ψ is set to zero as a reference.

2) At the melt/encapsulaant and melt/crystal interfaces,

$$\psi=\frac{1}{2}\rho_s U_{amp} r^2 \tag{15}$$

$$\omega=\frac{\partial u}{\partial z}-\frac{\partial v}{\partial r}$$

with

$$u=0, \qquad v=U_{amp}\rho_s/\rho_L \tag{16}$$

Since B_2O_3 is used as the encapsulant in this study, and its viscosity is two hundred times higher than that of the melt, the fluid flow in the encapsulant is thus neglected. As such, the no-slip boundary condition is adopted at the encapsulant/melt interface.

3) On the melt/ampoule interface,

$$\psi=\frac{1}{2}\rho_s U_{amp} R_{ai}^2, \qquad \omega=\frac{\partial u}{\partial z}-\frac{\partial v}{\partial r} \tag{17}$$

with

$$u=0, \qquad v=U_{amp}\rho_s/\rho_L \tag{18}$$

where R_{ai} is the inner radius of the ampoule as shown in *Figure 1*. Even though R_{ai} changes with distances, it is essentially constant in the melt zone considered in this report. Therefore, the streamline being a constant along the melt/ampoule is a reasonable assumption.

Although the initial mass of loaded material is known, the height of the melt/encapsulant interface still needs to be determined from the volumes of the melt and the crystal during crystal growth. Accordingly, this height of the melt/encapsulant interface, z_e, is determined from an overall mass balance:

$$\rho_s V_s+\rho_L V_L-m_o=0 \tag{19}$$

where V_s and V_L are the volumes of the crystal and the melt, and can be evaluated by simple

line integration[21]. Also, the depth of the encapsulant, d_e, is calculated by,

$$d_e = m_e/[\pi R_{ai}(z_e)^2 \rho_e]$$

In some design problems, direct calculation of the operation conditions for a flat interface, i.e., an inverse problem approach, could be very useful. To do this, we have chosen the cold-zone temperature T_C as a control parameter to justify the zero interface deflection condition:

$$h_c(R_{ai}) - h_c(0) = 0 \tag{20}$$

To this inverse problem, above equation provides a constraint (or an objective function), and T_C is an unknown parameter that needs to be determined. Some results for this inverse problem approach will be illustrated subsequently.

NUMERICAL METHOD

The above governing equations and boundary conditions are transformed into those in terms of general (nonorthogonal) curvilinear coordinates (η, ξ) which fit all the interfaces, as shown in *Figure 2*. Computatin is performed in the (η, ξ) domain. In this way, all the boundary conditions can be treated easily and accurately, as already described previously[21–23].

The equation of motion, the stream equation, and the energy conservation equation ((1)–(3)) are discretized by employing a finite-volume approach. The physical domain, in (r, z), is subdivided

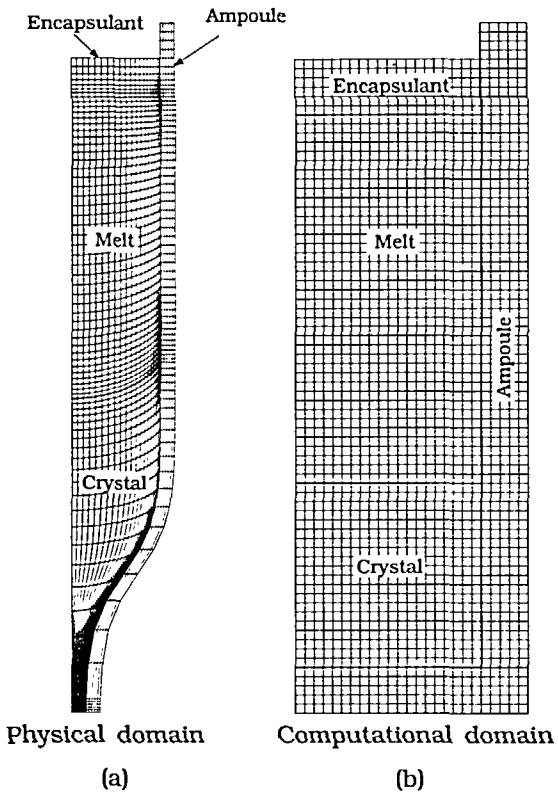

Figure 2 A nonorthogonal body-fitted coordinate system used for computation: (a) physical domain; (b) computational domain. The heavy lines are the interfaces in the computational domain

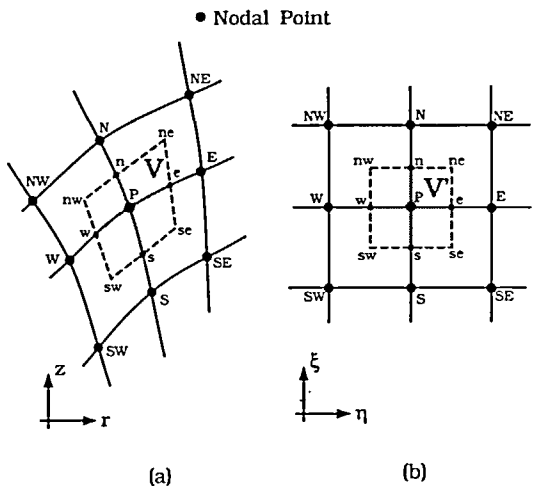

Figure 3 The arrangement of nodal points and finite volumes: (a) physical domain; (b) computational domain

into a finite number of contiguous volumes (*CVs*) of volume V, which are bounded by cell faces located about halfway between consecutive nodal points; see *Figure 3*(a). This domain can be transformed into a computation domain (η, ξ) with a CV of volume V', as shown in *Figure 3*(b), and $rdV = rJdV'$, where J is the Jacobian of coordinate transformation $(J = r_\eta z_\xi - r_\xi z_\eta)$. Now, the integration of these equations over the CV can be proceeded as follows:

$$\int_V [(1) \text{ to } (3)] r \, dV. \tag{21}$$

After the Gauss theorem is applied, the above equation can be transformed into surface integrals (fluxes) over the faces of CV. The resulting balance equations for each CV can then be expressed as,

$$I_e - I_w + I_n - I_s + \int_{V'} (dJ) \, d\eta \, d\xi = 0, \tag{22}$$

where I_e, for example, represents the total flux of field variable (ψ, ω, and T) across the face e, and d the source term in (1)–(3)[21]. Equation (22) involves no approximation and represents the finite-volume equation of the differential equations. The numerical evaluation of the different terms in (22) requires the calculation of geometrical factors for control volumes and a discretization scheme for interpolating quantities at the cell faces from their adjacent nodal values. The details of the discretization scheme can be found elsewhere[21]. Boundary conditions are discretized by the second order finite differences.

After these discretizations for both governing and boundary equations, a set of nonlinear equations can be obtained,

$$\mathbf{f}(\mathbf{x}) \equiv \mathbf{f}(T, \psi, \omega, h_c, z_e, T_C) = 0, \tag{23}$$

where h_c and z_e are the heights of melt/crystal and melt/encapsulant interfaces; see *Figure 1*. T_C needs to be solved only when (20) is imposed. The above nonlinear equation set is solved by Newton's method for the field and interface variables simultaneously. Starting from an initial approximation to vector of unknowns $\mathbf{x}^0$, successive updates are constructed as,

$$\mathbf{x}^{n+1} = \mathbf{x}^n + \delta^{n+1}, \tag{24}$$

where the correction vectors δ^{n+1} is the solution of the linear equation set,

$$\tilde{\mathbf{J}}\delta^{n+1} = -\mathbf{f}(\mathbf{x}^n). \tag{25}$$

The components of the Jacobian matrix $\tilde{\mathbf{J}}$, formed by explicit differentiation as $\tilde{J}_{ij} \equiv \partial f_i/\partial x_j$, represent the sensitivity of the residual vector to the solution vector. They are obtained, mostly, by the finite-difference approximation with consideration of the sparse structure of $\tilde{J}$, so that the number of function evaluations can be minimized[24]. The components of $\tilde{J}$ for the overall mass balance, (19), are evaluated analytically. The dependence of the residual equations on the unknowns gives $\tilde{J}$ an 'arrow-shape" structure typical of free-boundary problems[25]. Equation (25) is solved by the *GMRES* iterative linear equation solver[26] with a preconditioner for the incomplete *LU* decomposition without fill-in, *ILU*(0)[27]. In the implementation of Newton's scheme, continuation can play a vital role, particularly when the solution behavior changes dramatically with small changes in one or more of parameters. Hence, the pseudo arc length continuation[28] is also used to locate the results from one to the other.

Although the interface variable h_c is solved with other field variables simultaneously, two formulations for h_c can be used: one is to use the Stefan boundary condition, i.e., (8), and the other is the isotherm condition, i.e., (9). However, since h_c does not appear explicitly in the isotherm condition, the former approach is found to be more robust during *GMRES* iterations. The detailed description of the numerical implementation can be found elsewhere[21].

RESULTS AND DISCUSSION

Validation of the model

The single crystal growth of *GaAs* in a pyroltic boron nitride (*PBN*) ampoule with B_2O_3 as the encapsulant is used to demonstrate the steady-state calculations of the LEVB process. Before the demonstration of the effects of process parameters, a simple comparison of present calculations with FEM calculations of Adornato and Brown[8] for germanium crystal growth in a graphite ampoule (R_{ai}=0.7 cm) is performed; $U_{amp} = -4 \times 10^{-4}$ cm/s. In *Figure 4*, the flow patterns and the interface shape for two different thermal Rayleigh numbers ($Ra_T = g\beta_T \Delta T z_L^3/\mu\alpha$) are demonstrated; $\Delta T = T_H - T_C$ and α is the thermal diffusivity. The ambient temperature distribution is shown on the RHS and is linear. In each figure, the LHS shows the streamlines and the RHS the isotherms. The temperature distributions, the single-cell flow structure, and the melt/crystal interface shape are in good agreement with the FEM results[8]; the streamlines due to crystal growth in *Figure 4*(b) were not shown in previous report. The maximum and minimum of the stream functions (ψ_{max} and ψ_{min}) are indicated by a plus and a minus, respectively, while the maximum of temperature (T_{max}) by a cross. The streamlines are equally spaced at $\Delta\psi = \psi_{max}/10$ for positive ones and at $\Delta\psi = \psi_{min}/10$ for negative ones. The isotherms are also equally spaced at $\Delta T = (T_{max} - T_m)/10$ in the melt and the solid. These definition of $\Delta\psi$ and ΔT will be used throughout this study unless otherwise stated. The discrepancy in maximum of streamlines with FEM results is mainly due to different definitions of the stream function (without ρ_L in Reference 8). The convergence of *Figure 4*(b) is also demonstrated in *Figure 5*. The ambient temperature distribution and zero stream function and vorticity are used as an initial guess. As shown, a quadratic convergence is achieved. CPU time required for a Newton's iteration takes only about 20 s in the HP9000/735 workstation. For all cases in this study, the calculations converge to an infinity norm of 1×10^{-6} for both correction and residual vectors within five iterations. Due to the quadratic convergence of the method, the convergence error in the present calculations can be neglected. As shown, the computation time required for the pseudo steady-state approach is quite short, which is favoured by a real-time controlled model-based crystal growth system.

In addition to the convergence error, the numerical simulation can also be suffered by the discretization error; sometimes, results from coarse meshes may lead to wrong conclusions.

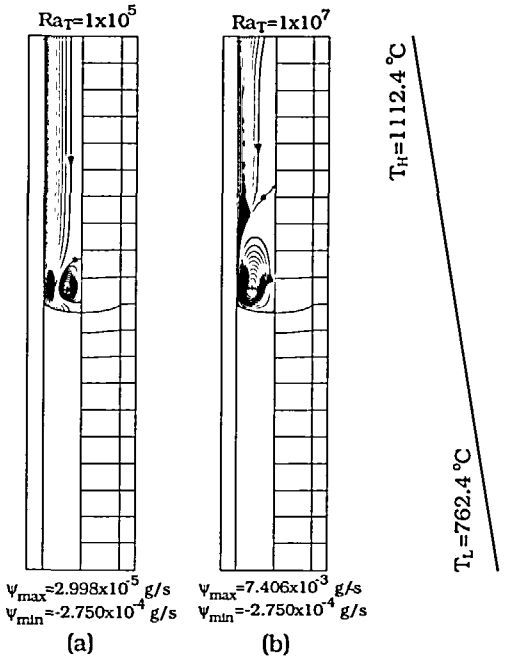

Figure 4 The calculated results for germanium/graphite system[8] at two different Rayleigh numbers: (a) $Ra_T = 1 \times 10^5$; (b) $Ra_T = 1 \times 10^7$. The effective ambient temperature distribution is linear and shown on the RHS

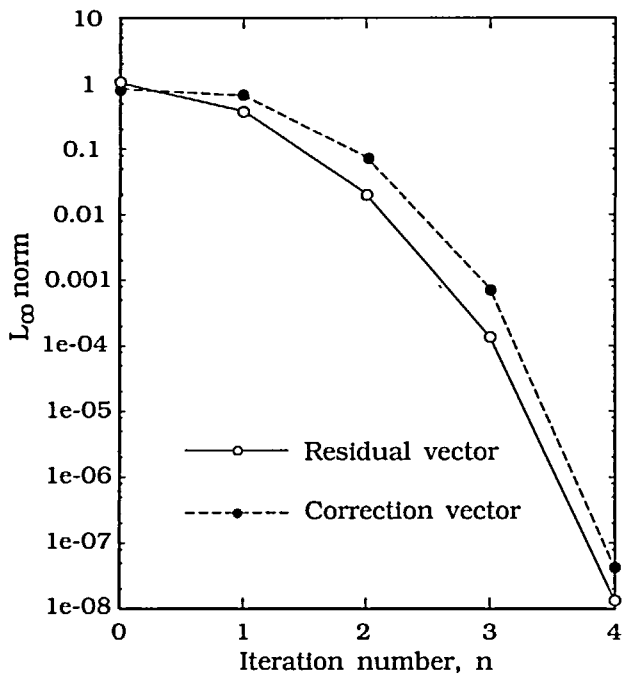

Figure 5 Convergence of Newton iteration scheme for *Figure 4*(b) ($Ra_T = 1 \times 10^7$)

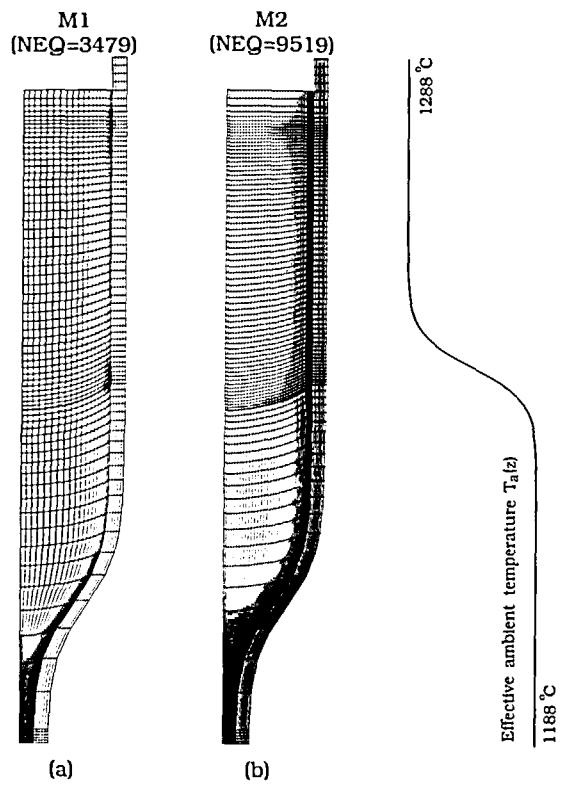

Figure 6 The different grids used for LEVB growth of *GaAs* in *PBN* crucible: (a) number of grid points = 1896 and number of equations (NEQ) or unknowns = 3479; (b) number of grid points = 4736 and *NEQ* = 9515. The effective ambient temperature distribution is shown on the RHS

Fortunately, this error can usually be examined through mesh refinements. On the other hand, calculations with a finer mesh need more CPU time and memory of computer. The effect of mesh on the accuracy of calculation is examined through two different meshes for $GaAs/B_2O_3/PBN$ system. *Figure 6* shows two different meshes used for computation. The physical properties of materials and input parameters used are listed in *Table 1*, and will be used throughout this report unless otherwise stated. In the present calculation, an isotropic *PBN* ampoule is adopted[8], and the radiation is neglected ($\varepsilon_a = 0$). The effects of radiation (nonzero ε_a) on the flow patterns and interface morphology will be considered shortly for comparison. In *Figure 6*, the numbers of grids and unknowns are 1896 and 3479 for mesh M1 in *Figure 6*(a) and are 4736 and 9519 for mesh M2 in *Figure 6*(b), respectively. The effective ambient temperature is also shown on the RHS of *Figure 6*, in which $T_H = 1288°C$, $T_C = 1188°C$, $a = 2$ cm, and $z_p = 5.5$ cm. The calculated results based on the meshes M1 and M2 are shown in *Figure 7*(a) and *Figure 7*(b), respectively. Apparently, the calculated results shown in *Figure 7*(a) and *Figure 7*(b) are very close to each other; in fact, the differences in ψ_{max}, ψ_{min}, and T_{max} are within 1.2%. Therefore, the calculations are quite independent of the meshes so far. Although the coarser mesh M1 in *Figure 6*(a) seems to be satisfactory for the calculations, the finer mesh M2 in *Figure 6*(b) is still chosen for the rest of study. Again, one Newton's iteration takes only about 40–50 s for mesh M2.

Table 1 Physical properties and input parameters[29-31]

GaAs	B_2O_3	*PBN*	*Other input parameters*
$\rho_s = 5.17$ g cm^{-3}	$\rho_e = 1.648$ g cm^{-3}	$\rho_a = 2.3$ g cm^{-3}	$R_{ai} = 0.2 + 0.535(1 + \tanh[1.3(z-2)]/\tanh[2.6])$ cm
$\rho_L = 5.71$ g cm^{-3}	$k_e = 2 \times 10^{-2}$ W cm^{-1} °C^{-1}	$h = 0.1$ W cm^{-2} °C^{-1}	$R_{ao} = R_{ai} + 0.2$ cm
$T_m = 1238$°C	$Cp_e = 0.48$ J g^{-1} °C^{-1}	$k_a = 2.6 \times 10^{-1}$ W cm^{-1} °C^{-1}	$z_L = 10$ cm
$\Delta H = 726$ J g^{-1}	$m_e = 4.175$ g	$Cp_a = 1.9$ J g^{-1} °C^{-1}	$T_H = 1288$°C
$h = 0.1$ W cm^{-2} °C^{-1}		$\varepsilon_a = 0.0$ or 0.8	$T_C = 1188$°C
$k_S = 7.0 \times 10^{-2}$ W cm^{-1} °C^{-1}			$a = 2$
$k_L = 1.4 \times 10^{-1}$ W cm^{-1} °C^{-1}			$z_p = 5.5$ cm
$Cp_s = Cp_L = 0.42$ J g^{-1} °C^{-1}			
$\mu = 0.01967$ g cm^{-1} s^{-1}			
$\beta_T = 1.16 \times 10^{-4}$ °C^{-1}			
$m_0 = 190$ g			

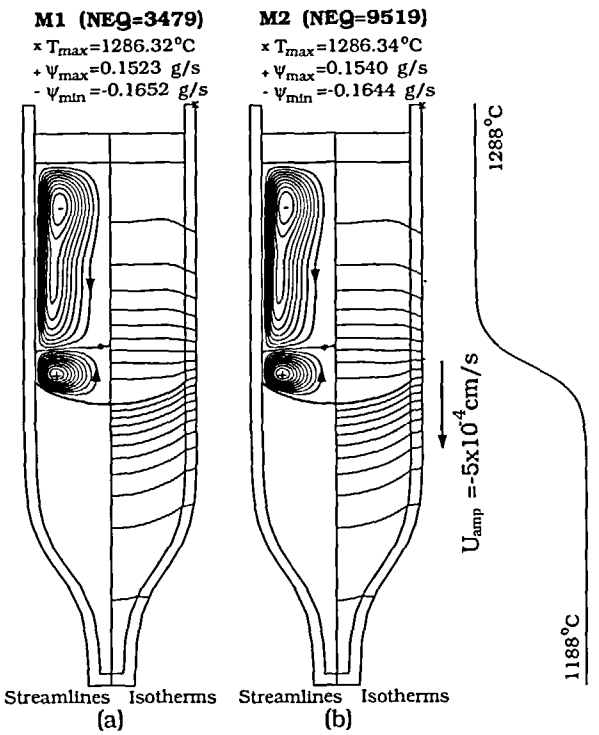

Figure 7 Calculated results based on the grids in: (a) *Figure 6*(a), (b) *Figure 6*(b). The LHS is the streamlines and the RHS isotherms. $\Delta\psi = \psi_{max}/10$ for positive ψ (+), $\Delta\psi = \psi_{min}/10$ for negative ψ (−), $\Delta T_m = (T_{max} - T_m)/10$ and $\Delta T_s = \Delta T_m$. Zero streamline is indicated by an asterisk (*) and T_{max} a cross (×)

Effect of growth rate

When a pseudo steady-state is reached, the crystal growth rate is equal to the ampoule pulling speed U_{amp}. *Figure 8* illustrates the effect of crystal growth rate or the ampoule pulling speed. The ampoule speeds (downwards) are 0, -5×10^{-4} cm/s, and -2×10^{-3} cm/s in *Figures 8*(a), *8*(b) and *8*(c). respectively. As shown, the interface position shifts downward as the $|U_{amp}|$ increases. Meanwhile, the concavity of the melt/crystal interface, as well as the size and the intensity of the lower convection cell, increases with the increasing $|U_{amp}|$. However, the maximum temperature and the intensity of the upper flow are not affected by the pulling speed much. In each case, there are two convection cells in the melt, which is a typical flow structure for the VB system[8]. The direction of the upper cells is clockwise, which is induced by radial temperature gradients, while the lower cell, due to the interface deflection, is counterclockwise in direction. According to Adornato and Brown[8], the convection of the upper loop is mainly induced by thermal imperfection between the ampoule and the ambient, and also the thermal conductivity difference between the melt and ampoule. The lower cell is induced by the mismatch of thermal conductivity of melt and crystal. However, it should be pointed out that the lower cell still exists even though the thermal conductivities of the melt and the crystal are set to be equal. In fact, heat of fusion releases as the solidification proceeds. The higher the growth rate, the more the latent heat is released. The latent heat also makes the melt near the growth front hotter and thus lowers the temperature gradients and the melt/crystal interface there. Meanwhile, the radial temperature gradients and the deflection of the melt/crystal interface also increase due to radial cooling. The effect of growth rate on the axial temperature is further demonstrated in *Figure 9*,

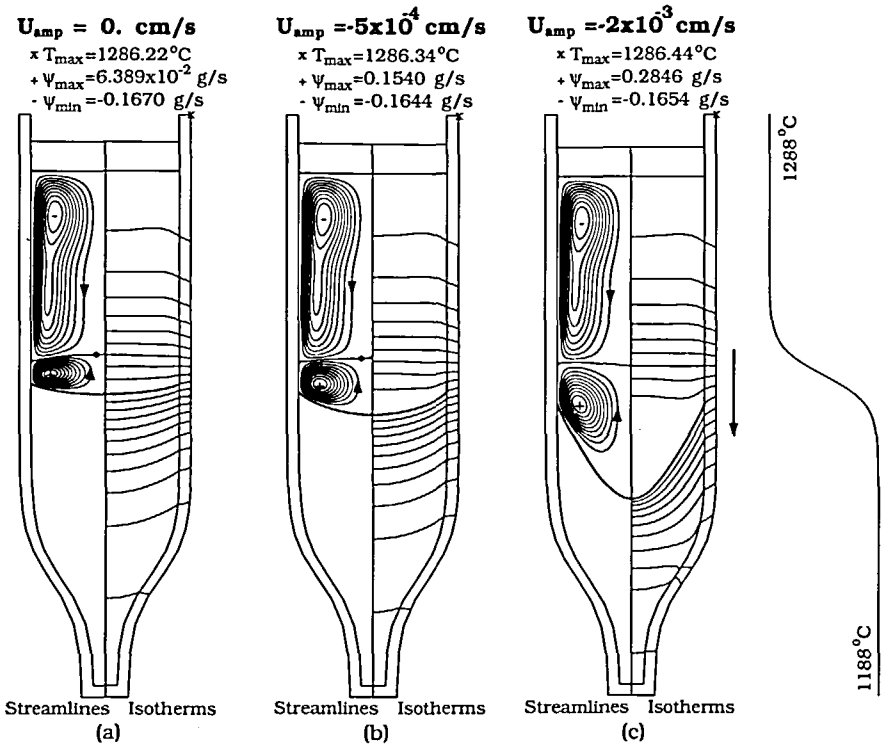

Figure 8 Effect of ampoule pulling speed: (a) $U_{amp}=0$ cm/s; (b) $U_{amp}=-5\times10^{-4}$ cm/s; (c) $U_{amp}=-2\times10^{-3}$ cm/s

in which the temperature distributions along the centreline at different growth rates are presented. As shown, at $U_{amp}=0$, there is the discontinuity in the temperature gradient at the melt/crystal interface, and this is due to the difference in the thermal conductivities of melt and crystal. When $|U_{amp}|$ is increased, the discontuinity increases; the gradient decreases in the melt but increases in the solid. At $U_{amp}=-2\times10^{-3}$ cm/s, near the melt/crystal interface the temperature gradient in the melt becomes very small. In fact, the maximum growth rate can be found by extrapolating the calculated temperature gradient at the melt side to zero. For a crystal growth rate higher than 2×10^{-3} cm/s, the convergence is not possible in the present calculation.

Effect of ambient temperature profile

Setting an optimum furnace temperature profile for LEVB crystal growth may be the most challenging task to crystal growers. In a traditional VB furnace, two temperature zones are used, and between two zones there is an adiabatic zone to regulate the temperature gradients near the melt/crystal interface and thus control the growth front (melt/crystal interface). Even for the multi-zone furnace VDGF technique, the setting of the temperature profile can also be very complicated. So far, no general rules have been reported for setting an optimal furnace temperature profile. However, the traditional two-zone VB furnace and the gradient furnace (with a linear heating profile) have been widely used because of their simple design. To give a simple comparison of these two furnaces, two types of temperature profiles are considered here, and the calculated results are shown in *Figure 10*. The ambient temperature profiles are also shown on the RHS of each figure. In *Figure 10*(a), the temperature distribution is described by a hyperbolic tangent function, (13), where $a=2$ is used to make a larger temperature gradient near the melt/crystal interface. In *Figure 10*(b), a linear temperature profile is used. For both figures,

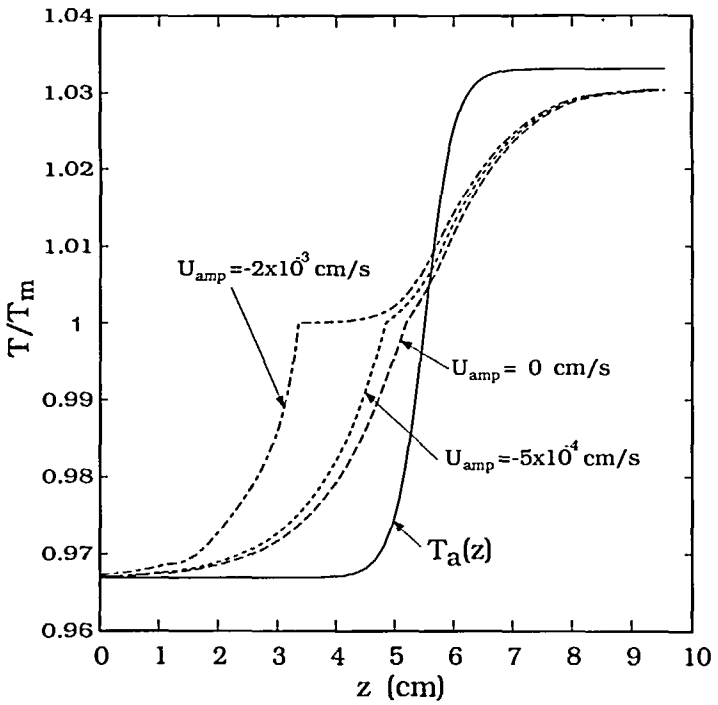

Figure 9 Axial temperature profile along the centerline ($r=0$) at different ampoule pulling speeds (from *Figure 8*)

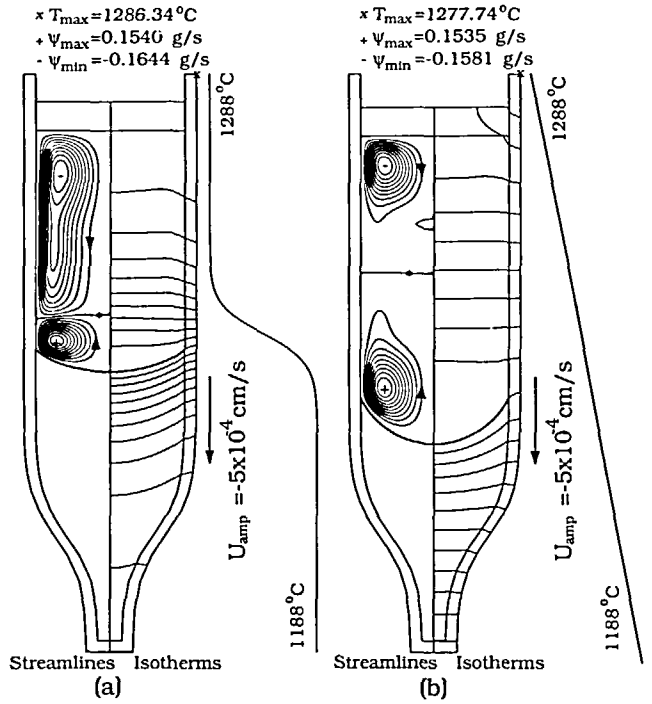

Figure 10 Effect of ambient temperature distribution at $U_{amp} = -5 \times 10^{-4}$ cm/s; (a) a hyperbolic tangent function, (b) a linear function

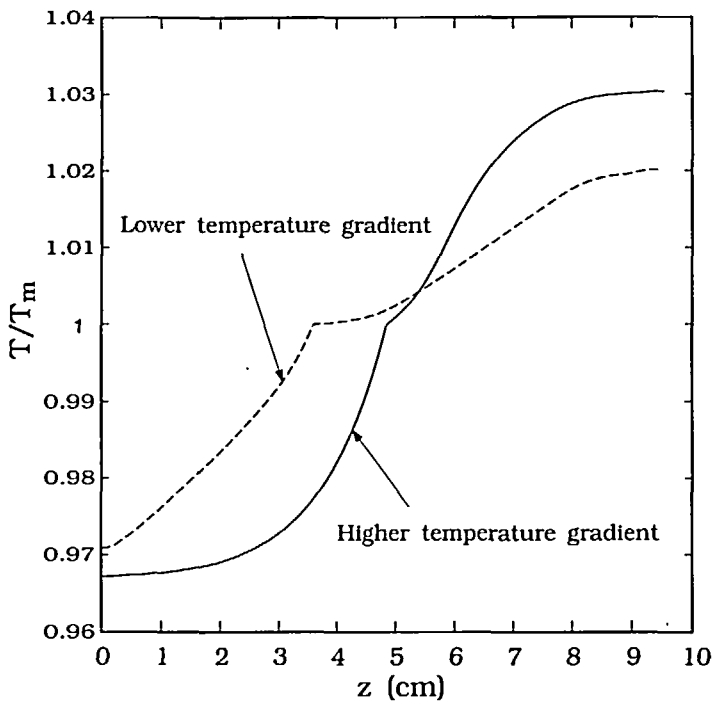

Figure 11 Axial temperature profile along the centerline ($r=0$) at different ambient temperature profiles (from *Figure 10*); $U_{amp} = -5 \times 10^{-4}$ cm/s

the same temperature difference, $T_H - T_C = 100°C$, is used for comparison. As shown, due to crystal growth, the melt/crystal interface shifts downward and becomes more concave for both heating profiles. However, the change is much more significant in *Figure 10*(b), where a linear ambient temperature profile is used. As a result of the more concave growth front, the size of the lower convection cell increases. Similar results can be found in Adornato and Brown[8]. The temperature distributions along the centerline are also illustrated in *Figure 11*. As shown, the temperature gradient near the growth front with the linear temperature profile is much smaller than that with the hyperbolic tangent profile. Clearly, with a linear temperature profile the removal of heat of fusion may be more difficult due to smaller temperature gradients. Thus a lower and more deflected melt/crystal interface is needed to accommodate the heat of fusion. In other words, with the same hot- and cold-zone temperatures and the growth speed it may be easier to obtain a flat interface in the traditional VB two-zone furnaces.

Effect of radiation

So far, the radiative heat transfer between the furnace and the ampoule is neglected by setting $\varepsilon_a = 0$ for simplicity. However, in a high temperature system the radiative heat transfer, usually, is important and cannot be ignored. To demonstrate this effect, calculations with $\varepsilon_a = 0.8$ are performed for comparison. As shown in *Figure 12*, results from two emissivity values, $\varepsilon_a = 0$ and 0.8, are compared. Clearly, T_{max} increases slightly when the radiation is considered, but its effect on the convection and the growth front shape is not significant. From the isotherms, it can also be observed that with radiation the temperature in the melt is slightly higher, while in the crystal is lower. It should be pointed out that in a real crystal growth furnace, the effective thermal profile can be affected significantly by the radiation exchanges in the whole system, including

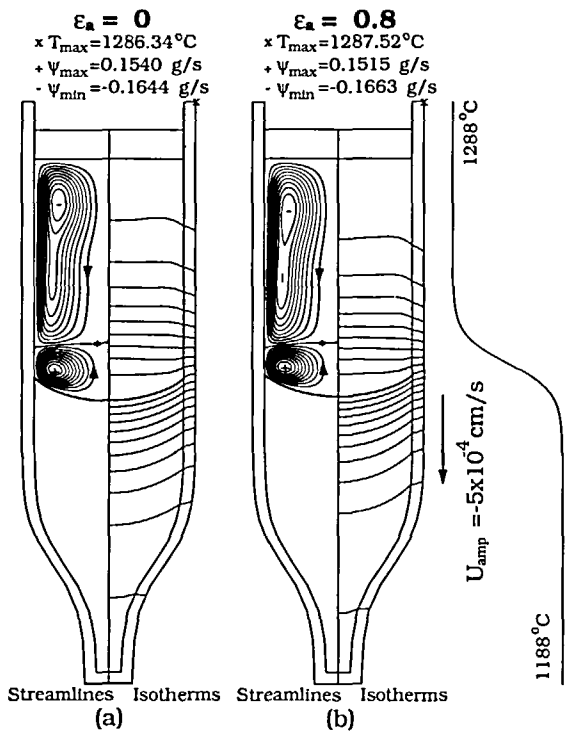

Figure 12 Effect of emissivity of ampoule: (a) $\varepsilon_a = 0$; (b) $\varepsilon_a = 0.8$. $U_{amp} = -5 \times 10^{-4}$ cm/s and $h = 1000\ \mathrm{Wm^{-2}\,K^{-1}}$

the furnace. Unfortunately, the global modelling of the radiative heat transfer is not taken into account in this study. Therefore, the effect of radiation is still not clear, but at least the effect of emissivity is not significant in this case. In the following discussion, the effect of emissiviity is considered, and $\varepsilon_a = 0.8$ will be used for the rest of calculations.

Interface control

As mentioned earlier, a flat or slightly convex melt/crystal interface is desired for crystal growth in the LEVB process. However, the cases discussed so far have only concave melt/solid interfaces. Nevertheless, from the effect of the ambient temperature profile in the previous section, it may be reasonable to say that the higher the temperature gradient, the less concave the melt/crystal interface is. Therefore, using a higher ambient temperature gradient in the system near the melt/crystal interface may be a right direction to achieve a flat or convex interface. This idea is further demonstrated in *Figure 13* by lowering T_C, while the distribution function is unchanged; however, the position of T_m in the distribution is shifted upward slightly. As shown in *Figure 13*, the interface position shifts upward and its shape becomes much less concave with decreasing T_C (or increasing the temperature gradient). Due to the less concave interface, the lower flow cell becomes weaker and its intensity smaller. For example, the intensity of the lower flow cell in *Figure 13*(b) is now two orders of magnitude smaller than that in *Figure 13*(a). Interestingly, when T_C is lowered down to 888°C in *Figure 13*(c), the growth front becomes convex, and the lower cell disappears. The inversion of the melt/crystal interface by increasing the temperature gradient in the crystal was also observed in the simulation and crystal growth practice by Hofmann *et al.*[17]. Although the interface position related to the adiabatic zone is also an important factor to the interface inversion[32], high enough temperature gradients in the crystal near the melt/crystal

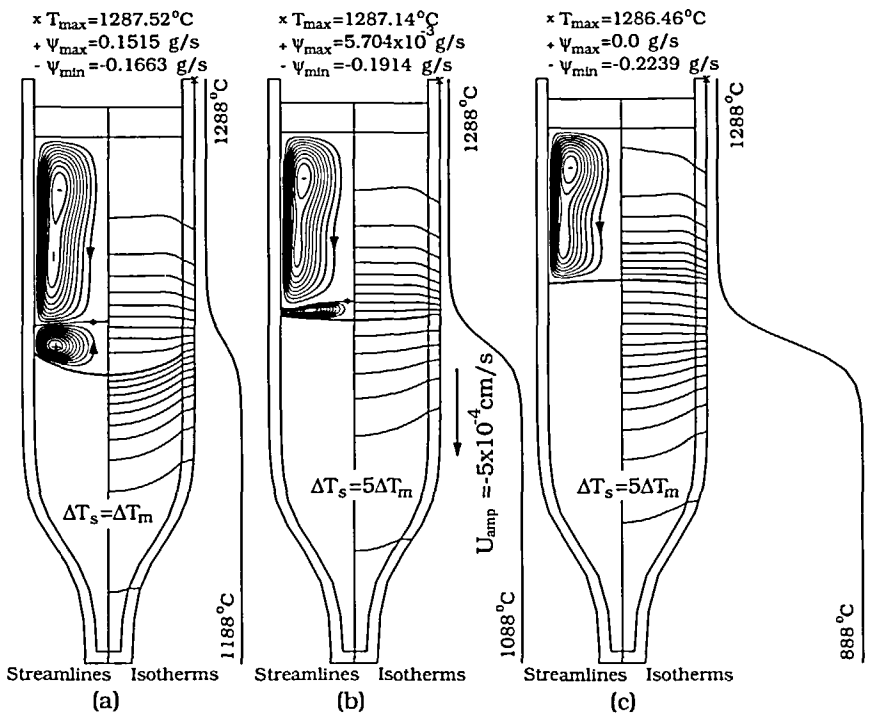

Figure 13 Effect of cold-zone temperature: (a) $T_C = 1188°C$; (b) $T_C = 1088°C$; (c) $T_C = 888°C$. $U_{amp} = -5 \times 10^{-4}$ cm/s, $h = 1000\ \mathrm{Wm^{-2}\,K^{-1}}$, and $\varepsilon_a = 0.8$

interface are still required to remove the heat of fusion effectively. On the other hand, the temperature gradients in the crystal cannot be increased too much, especially in the case of *GaAs* due to its lower critical resolved shear stress (CRSS). The thermal stress induced defects could be a serious problem. Therefore, in addition to interface control, the control of thermal gradients in the crystal is important as well. In the following sections, an effective way to obtain a flat interface, and at the same time to find a condition with smaller temperature gradients in the crystal, is illustrated.

Conditions for a flat interface

From process design point of view, it may be more useful to calculate a right growth condition (e.g., T_C) directly for a flat interface without trial-and-error. An efficient way to do so is through an inverse problem approach. The inverse problem approach used here is quite simple. We simply impose a zero deflection condition, (20), and solve the operation parameter T_C together with all other field variables using the robust Newton's scheme. In fact, for the VB crystal growth, the interface shape is usually very simple. As it is, the zero interface deflection condition is a good approximation to a flat interface. As compared with the approach used by Tortorelli *et al.*[20], this approach is better conditioned and much easier to be implemented. This approach has proven to be effective for the cases with different hot-zone temperatures (T_H), and some of sample results are shown in *Figure 14*. As shown, due to the flat interface, there is only one main flow cell in the melt; the extremely small secondary flow cell near the lower corner can be neglected. More interestingly, the lower the T_H, the higher the T_C can be used for obtaining a flat interface. The flow is also weaker at lower T_H. Their axial temperature distributions at the centerline are further demonstrated in *Figure 15*. Obviously, if a lower hot zone temperature is

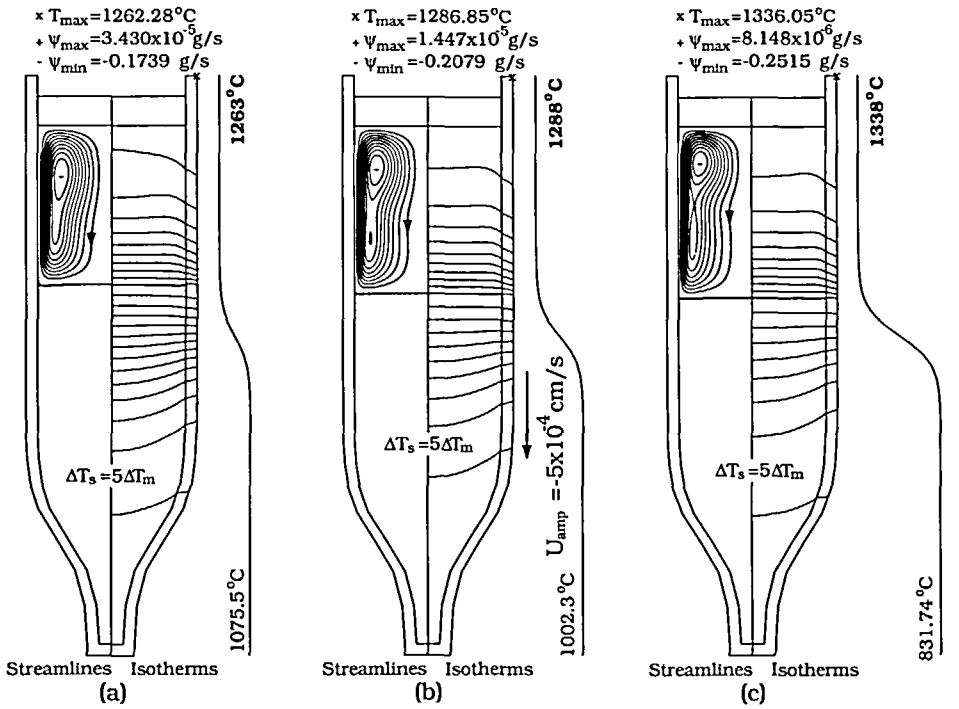

Figure 14 Effect of hot-zone temperature for the flat interface condition: (a) $T_H = 1263°C$; (b) $T_H = 1288°C$; (c) $T_H = 1338°C$; $U_{amp} = -5 \times 10^{-4}$ cm/s

used, temperature gradients in the crystal are also smaller, which is favoured for growing single crystals with a lower dislocation density.

In the traditional VB process, changing the adiabatic zone length, which can be characterized by the parameter a in $T_a(z)$, is also an effective way to control interface morphology. *Figure 16* shows the results for a flat interface at various a. Clearly, if the temperature gtadient is higher (larger a) near the interface, a higher T_C value can be used for a flat interface. Their axial temperature distributions at the centerline for various a are further illustrated in *Figure 17*. Interestingly, the calculated temperature gradients for various a are very close to one another in the crystal near the interface.

The last example for interface control is the effect of a booster heater. The idea of using a radial booster heater was originally proposed by Jasinski and Witt[33], and was further applied in a realistic furnace design by Koai *et al.*[34]. To illustrate the effect of local heating from the booster heater, we applied an overshoot heating profile to the system. *Figure 18* shows the calculated results with various local heating, which is represented by the overshoot temperature ΔT_p. In all of the cases, the hot-zone temperature is kept only 10°C higher than the melting point. *Figure 18*(a) illustrates the case without local heating ($\Delta T_p = 0$). As shown, the interface is quite flat, but concave near the melt/ampoule interface. The concave interface near the ampoule can induce parasitic nucleation and lead to polycrystals. However, as the booster heater is turned on and set $\Delta T_p = 25°C$ (*Figure 18*(b)), the interface becomes very flat; the interface deflection is zero. More interestingly, as the local heating is increased further, as shown in *Figure 18*(c), the interface becomes slightly concave. The concave interface due to the booster heater has not been reported before. Meanwhile, the maximum temperature is now located at the middle of the sample, and this results in larger radial temperature gradients in the melt. As it is, the convection in the melt becomes much stronger, and the flow structure becomes two-cell. The stronger flow

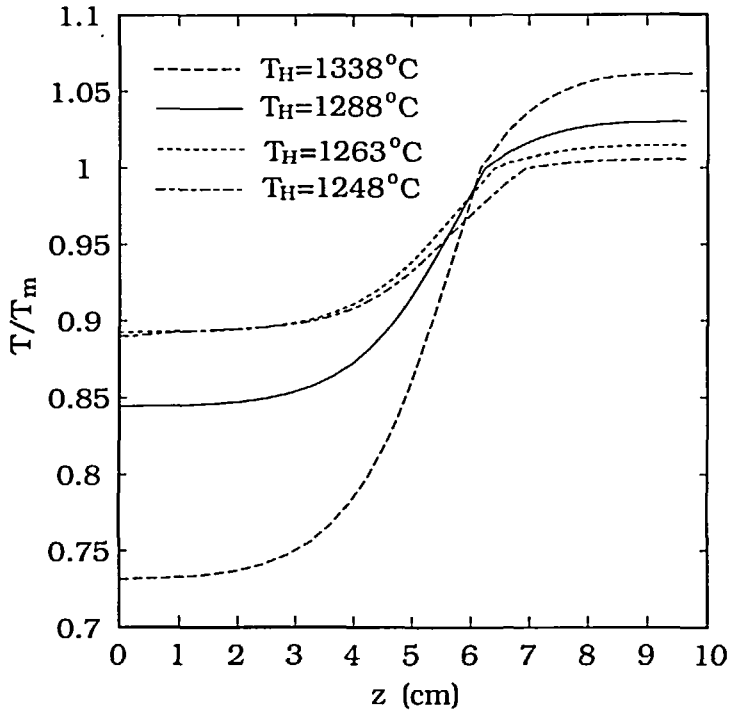

Figure 15 Axial temperature profile along the centerline ($r=0$) at different hot-zone temperatures (from *Figure 14*) for the flat interface condition; $U_{amp} = -5 \times 10^{-4}$ cm/s

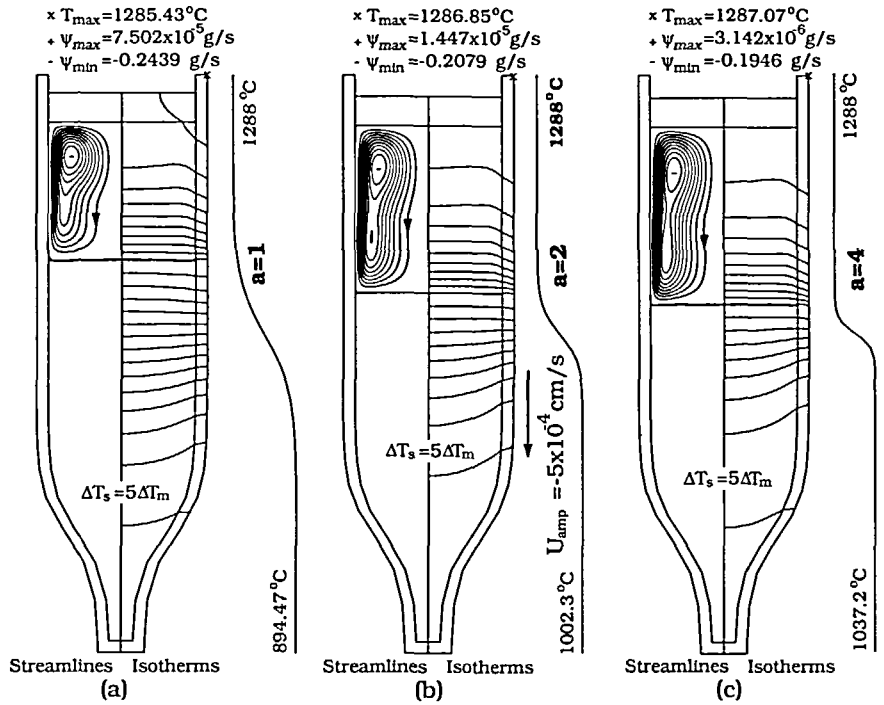

Figure 16 Effect of adiabatic zone length for the flat interface condition: (a) $a=1$; (b) $a=2$; (c) $a=4$; $U_{amp} = -5 \times 10^{-4}$ cm/s

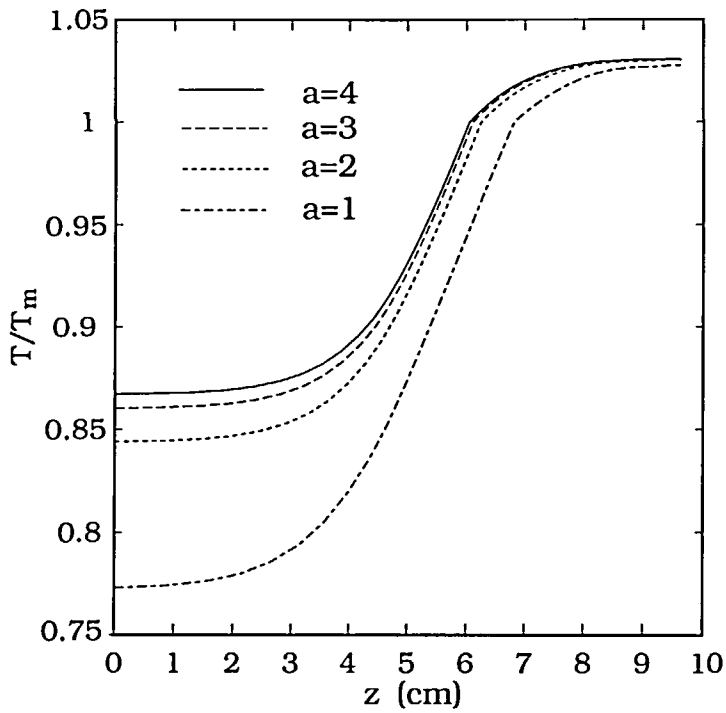

Figure 17 Axial temperature profile along the centerline ($r=0$) at different adiabatic zone length (from *Figure 16*) for the flat interface condition; $U_{amp} = -5 \times 10^{-4}$ cm/s

and the two-cell flow structure induced by the booster heater were also observed by Neugebauer and Wilcox[35] in the flow visualization of VB salol growth. Therefore, from this example it is clear that a careful tuning of the local heating is required to obtain a satisfactory result. Finally, it should be pointed out that, with the help of the booster heater at $\Delta T_p = 25°C$, the cold-zone temperature for a flat interface can be elevated to 1122.7°C, as compared to the case in *Figure 14*(a) (1075.5°C).

CONCLUSIONS

1) A pseudo steady-state model, which simulates heat transfer and fluid flow, as well as the melt/crystal interface, is used to study the liquid encapsulated vertical Bridgman crystal growth. A finite-volume/Newton method is used to solve this model. The calculated results for *Ge/graphite* system are in good agreement with the previous report. The quadratic convergence of the method and mesh refinements are also illustrated. The effects of process prameters for $GaAs/B_2O_3/PBN$ system are demonstrated through calculated results.

2) Two-cell flow structure is observed for crystal growth with a concave melt/crystal interface, and this is consistent with previous numerical studies for the vertical Bridgman process. Furthermore, the higher the growth rate, the more concave the melt/crystal interface is. Due to the larger interface deflection, the lower convection cell becomes larger at a higher growth rate. Calculations also show that a linear ambient temperature profile, which is commonly used in a gradient freeze furnace, may lead to a more concave melt/crystal interface.

3) In the present study, when the effective ambient temperature distribution is assigned, the effect of emissivity (radiation) is not significant. However, in practice the effective ambient temperature profile is affected by the radiative heat transfer exchange in the whole system. The detailed

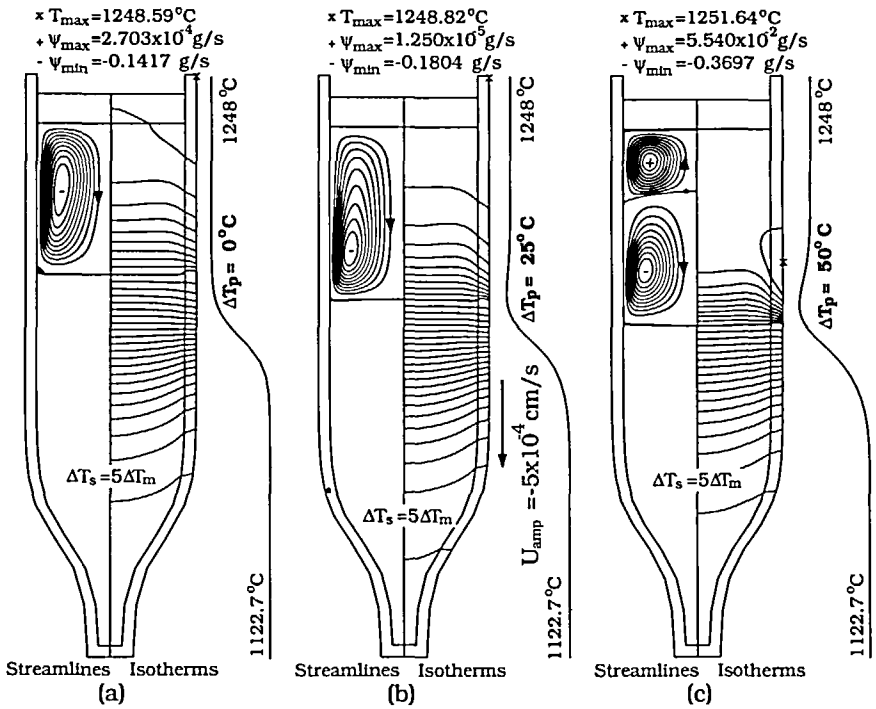

Figure 18 Effect of the booster heater: (a) $\Delta T_p = 0°C$; (b) $\Delta T_p = 25°C$; (c) $\Delta T_p = 50°C$; $U_{amp} = -5 \times 10^{-4}$ cm/s

design and the materials of the furnace, including heating elements, insulation, etc., can all affect the results. Therefore, the effect of radiation is still not clear.

4) A flat or a convex growth front can be obtained if the gradient of the ambient temperature profile is large enough, and the position of the melt/crystal interface is located near the upper edge of the adiabatic zone. One-cell flow structure is observed for the case with a convex growth front.

5) The cold-zone temperature for the flat interface can be calculated directly through an inverse problem approach. Some sample results indicate that to obtain a flat interface if the hot-zone temperature or the adiabatic zone length is reduced, a higher cold-zone temperature can be used. Also, with the help of a booster heater near the interface, the cold-zone temperature can be further increased. However, too much local heating will lead to stronger convection, and sometimes produce a more concave interface.

ACKNOWLEDGMENTS

The authors are grateful for the support of National Science Council of the Republic of China under Grant No. NSC84-2215-E008-011.

REFERENCES

1 Hoshikawa, K., Nakanishi, H., Kohda, H. and Sasaura, M. Liquid encapsulated, vertical Bridgman growth of large diameter, low dislocation density, semi-insulating GaAs, **94**, 643–650 (1989)
2 Gault, W. A., Monberg, E. M. and Clemans, J. E. A novel application of the vertical gradient freeze method to the growth of high quality III-V Crystals, *J. Crystal Growth*, **74**, 491–506 (1986)
3 Clemans, J. E., Ejim, T. I., Gault, W. A. and Monberg, E. M. Bulk III-V compound semi-conductor crystal growth, *AT&T Tech. J.*, **65**, 29–41 (1989)

4 Monberg, E. M., Gault, W. A., Simchock, F. and Dominguez, F. Vertical gradient freeze growth of large diameter, low defect density indium phosphide, *J. Crystal Growth*, **83**, 174–183 (1987)
5 Abernathy, C. R., Kinsella, A. P., Jordan, A. S., Caruso, R., Pearton, S. J., Temkin, H. and Wade, H. Growth and characterization of low defect GaAs by vertical gradient freeze, *J. Crystal Growth*, **85**, 106–115 (1987)
6 Matsumoto, F., Okano, Y., Yonenaga, I., Hoshikawa, K. and Fukuda, T. Growth of twin-free ⟨100⟩ InP single crystals by the liquid encapsulated vertical Bridgman technique, *J. Crystal Growth*, **132**, 248–350 (1993)
7 M. C. Flemmings, Solidification Processing, McGraw-Hill, New York, 53–54 (1974)
8 Adornato, P. M. and Brown, R. A. Convection and segregation in directional solidification of dilute and non-dilute binary allows: effects of ampoule and furnace design, *J. Crystal Growth*, **80**, 155–190 (1987)
9 Kim, D. H. and Brown, R. A. Models for convection and segregation in the growth of HgCdTe by the vertical Bridgman method, *J. Crystal Growth*, **96**, 609–627 (1989)
10 Sen, S., Konkel, W. H., Tighe, S. J., Bland, L., Sharma, S. R. and Taylor, R. E. Crystal growth of large-area single crystal CdTe and CdZnTe by the computer-controlled vertical modified-Bridgman process, *J. Crystal Growth*, **86**, 111–117 (1988)
11 Motakef, S. Thermoelastic analysis of GaAs in LEC growth configuration: III. Thermal condition for control of stresses in low pressure system, *J. Crystal Growth*, **96**, 201–216 (1989)
12 Crochet, M. J., Dupret, F., Ryckmans, Y., Geyling, F. T. and Monberg, E. M. Numerical simulation of crystal growth in a vertical Bridgman furnace, *J. Crystal Growth*, **97**, 173–185 (1989)
13 Kelly, K. W., Koai, K. and Motakef, S. Model-based control of thermal stresses during LEC growth of GaAs. 1. Validation of thermal-model, *J. Crystal Growth*, **113**, 254–264 (1991)
14 Brown, R. A. and Kim, D. J., Modelling of directional solidification: from Scheil to detailed numerical simulation, *J. Crystal Growth*, **109**, 50–65 (1991)
15 Kim, D. H. and Brown, R. A. Transient simulations of convection and solute segregationm of GaAs growth in gradient freeze furnace, *J. Crystal Growth*, **109**, 66–74 (1991)
16 Kim, D. H. and Borwn, R. A. Modelling of the dynamics of HgCdTe growth by the vertical Bridgman method, *J. Crystal Growth*, **114**, 411–434 (1991)
17 Hofmann, D., Jung, T. and Muller, G. Growth of 2 inch Ge:Ga crystals by the dynamical vertical gradient freeze process and its numerical modelling including transient segregation, *J. Crystal Growth*, **128**, 213–218 (1993)
18 Suzuki, T., Okano, Y., Hoshikawa, K. and Fukuda, T. Heat transfer during GaAs growth of bulk single crystal by the liquid encapsulated vertical Bridgman technique, *J. Crystal Growth*, **128**, 435–438 (1993)
19 Taghavi, K. and Duval, W. M. B., Inverse heat-transfer analysis of Bridgman crystal-growth, *Int. J. Heat Mass Transfer*, **32**, 1741–1750 (1989)
20 Tortorelli, D. A., Tiller, M. M. and Dantzig, J. A., Optimal-design of nonlinear parabolic-system. I. fixed spatial domain with application to process optimization, *Comput. Methods Appl. Mech. Eng.*, **113**, 141–155 (1994)
21 Lan, C. W. Newton's method for solving heat transfer, fluid flow and interface shapes in a floating molten zone, *Int. J. Num. Meth. Fluids*, **19**, 41–65 (1994)
22 Lan, C. W. and Kou, S. Heat transfer, fluid flow, and interface shapes in floating-zone crystal growth, *J. Crystal Growth*, **108**, 351–366 (1991)
23 Lan, C. W. and Kou, S. Effect of rotation on heat transfer, fluid flow, and interfaces in normal gravity floating-zone crystal growth, *J. Crystal Growth*, **114**, 517–535 (1991)
24 Coleman, T. F., Garbow, B. S. and More, J. J. Software for estimating sparse jacobian matrices, *ACM Trans. Math. Soft.*, **10**, 329–347 (1984)
25 Saito, H. L. and Scriven, L. E., Study of coating flow by the finite element method, *J. Comput. Phys.*, **42**, 53–74 (1981)
26 Saad, Y. and Schultz, M. H. GMRES: a generalized minimal residual algorithm for solving nonsymmetric linear systems, *SIAM J. Sci. Stat. Comput.*, **7**, 856–869 (1986)
27 Meijerink, J. A. and van der Vorst, H. A. An iterative solution method for linear systems of which the coefficient matrix is a symmetric M-matrix, *Math. Comp.*, **31**, 148–162 (1977)
28 Keller, H. B. Numerical solution of bifurcation and nonlinear eigenvalue problems, in P. H. Rabinowitz (ed.), *Applications of Bifurcation Theory*, Academic Press, New York, 359–384 (1977)
29 Li, J., Sun, J. and Saghir, Z. Buoyant and thermocapillary flow in liquid encapsulated floating-zone, *J. Crystal Growth*, **131**, 83–96 (1993)
30 Jordan, A. S. Estimated thermal diffusivity, Prandtl number and Grashof number of molten GaAs, InP, and GaSb, *J. Crystal Growth*, **71**, 551–558 (1985)
31 Jordan, A. S. Some thermal and mechanical properties of InP essential to crystal growth modeling, *J. Crystal Growth*, **71**, 559–565 (1985)
32 Fu, T. W. and Wilcox, W. R. Influence of insulation on stability of interface shape and position in the vertical bridgman-stockbarger Technique, *J. Crystal Growth*, **51**, 557–567 (1981)
33 Jasinski, T. and Witt, A. F., On control of the crystal melt interface shape during growth in a vertical Bridgman configuration, *J. Crystal Growth*, **71**, 295–304 (1985)
34 Koai, K., Sonnenberg, K. and Wenzl, H., Influence of crucible support and radial heating on the interface shape during vertical Bridgman GaAs growth, *J. Crystal Growth*, **137**, 59–63 (1994)
35 Neugebauer, G. and Wilcox, W. R., Convection in the vertical Bridgman-Stockbarger technique, *J. Crystal Growth*, **89**, 143–154 (1988)